Novel flux-weakening strategy considering the saturation effects for electric vehicles

Carlos Miguel-Espinar[1], Daniel Heredero-Peris[1], Oriol Subirats-Rillo[1], Xavier Escaler[2], Daniel Montesinos-Miracle[1]

[1] Centre d'Innovació Tecnològica en Convertidors Estàtics i Accionaments (CITCEA-UPC) ETS d'Enginyeria Industrial de Barcelona, Av. Diagonal 647, 08028 Barcelona, Spain
[2] Departament de Mecànica de Fluids, Universitat Politècnica de Catalunya BarcelonaTech (UPC), Av. Diagonal 647, 08028 Barcelona, Spain

Corresponding author: Carlos Miguel-Espinar, carlos.miguel@upc.edu

Abstract

This paper proposes an innovative control algorithm for Permanent Magnet Synchronous Machines (PMSMs), based on a Vector Current Control (VCC) strategy in order to operate in the Flux-Weakening (FW) zone and a Finite Element Analysis (FEA) to consider the cross-saturation effects. The proposed algorithm can be easily adapted either with or without the cross-magnetization outcome. The control algorithm includes the variation of the dq-axis inductances in the optimized problem of calculating the dq-axis currents from the torque setpoint. The simulation results verify the worthiness of the proposal for a 2.5 kW Surface Permanent Magnet Synchronous Machine (SPMSM) direct-drive e-motorbike.

1 Introduction

The growth integration of Permanent Magnet Synchronous Machines (PMSMs) in electric vehicle applications pushes the implementation of newer and more advanced control algorithms [1]. These control strategies go hand in hand with ingenious power converters to obtain the maximum available torque from the electric machine and increase its reliability in all speed ranges, regardless of the temperature and current conditions.

Authors in [2] classify different algorithms to obtain the maximum torque-speed capabilities of these machines by letting them work in the Flux-Weakening (FW) zone. Furthermore, some authors have proposed innovative FW algorithms capable of working in all the torque-speed extent, mainly in the deep FW region called Maximum Torque per Voltage (MTPV) [3]–[6]. The optimized working-point by taking into account the saturation cross-effects are only presented by default in two strategies: a direct open-loop algorithm with experimental look-up tables (LUTs) [3], [4], [7] and a torque and flux control method with LUTs [5]. The main drawback of these strategies is the mandatory dependency of experimental or Finite Element Analysis (FEA) results to calculate the dq-axis current references from the torque or speed setpoint.

Authors in [8] present a new control algorithm capable of working in all torque-speed characteristic points and commits to change from the torque to speed setpoint smoothly. However, the dq-axis inductances (L_d, L_q) are considered constant whatever the current is in the optimized calculation of the working-point from the torque or speed setpoint. This algorithm is based on a Vector Current Control (VCC) strategy, in which the reference voltage magnitude addresses the FW control by changing the current angle. Intrinsically, the main advantage of it is to take into account the resistor voltage drop and the saturation effects for the transition between the Low-Back Electromotive Force (LBEMF) and FW zones. Other authors have presented a similar approach, but they do not address the saturation consequences in the Constant Torque (CT), Current and Voltage Limit (CVL), and MTPV regions [6].

The main contribution of the proposed control algorithm is its simplicity if only the characteristic parameters are available, but at the same time its arrangement so as to get better results if the cross-

saturation effects of the machine are known. This paper proposes an integrated non-linear polynomial multi-variable approximation of the inductance variations regarding the currents of the machines in a VCC strategy. Moreover, a sensitivity analysis of the internal current control is carried out to study the instability of the controllers when the electric plant changes.

This paper is organised as follows. Section 2 analyses an FEA model, and presents the dq-axis inductance matrix and polynomial multi-variable equations. Furthermore, LBEMF and FW trajectories and the stability and dynamic response of the inner current controllers are analysed. In Section 3, the simulation model is shown, and the performance results are obtained to demonstrate the validity and accuracy of the proposed approach. Section 4 summarises the main conclusions.

2 Saturation Effects

2.1 Inductance evaluation by FEA

According to [9], the dynamic electrical equations that explain the performance of a PMSM related to the synchronous rotor frame at steady-state conditions are

$$V_d = R_\mathrm{s} I_d - \omega_\mathrm{e} L_q I_q \tag{1}$$

$$V_q = R_\mathrm{s} I_q + \omega_\mathrm{e} L_d I_d + \omega_\mathrm{e} \lambda_\mathrm{m}, \tag{2}$$

where V_d, V_q, I_d and I_q are the non time-dependent voltage and current dq components, L_d and L_q are the motor inductances at the dq frame, λ_m is the flux linkage which results due to the spinning of the magnets, R_s is the winding phase resistance, and ω_e is the non time-dependent electrical speed.

The electromagnetic torque (T_em) is expressed as

$$T_\mathrm{em} = \frac{3}{2}\mathrm{pp}(\lambda_\mathrm{m} I_q + (L_d - L_q) I_d I_q), \tag{3}$$

where pp is the pair of poles of the machine.

In general, the dq-axis inductances of the stator winding can be defined as

$$L_d = \left.\frac{\partial \lambda_d (I_d, I_q)}{\partial I_d}\right|_{I_q=0} + \left.\frac{\partial \lambda_d (I_d, I_q)}{\partial I_q}\right|_{I_d=0} \tag{4}$$

$$L_q = \left.\frac{\partial \lambda_q (I_d, I_q)}{\partial I_d}\right|_{I_q=0} + \left.\frac{\partial \lambda_q (I_d, I_q)}{\partial I_q}\right|_{I_d=0}, \tag{5}$$

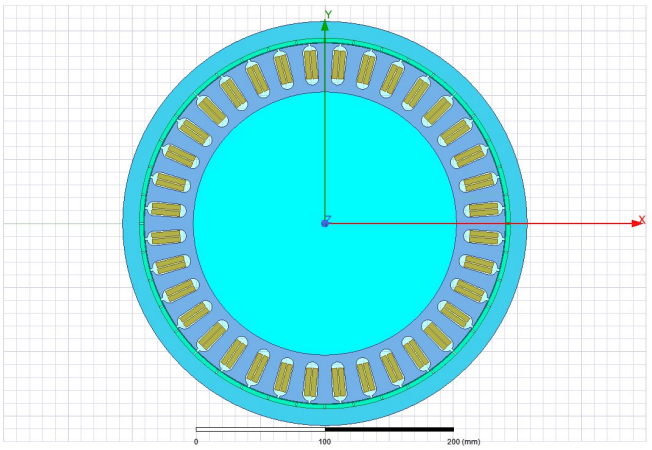

Fig. 1: Cross-section of a rotor-exterior SPMSM used in an electrical motorbike.

Tab. 1: Characteristic parameters of the analysed SPMSM

Symbol	Value	Unit	Description
R_s	17	mΩ	Phase resistor
L_d	81.75	μH	d-axis inductance
L_q	84.25	μH	q-axis inductance
λ_m	0.016	(V·s)/rad	Magnet flux-linkage
V_bat	48	V	Battery voltage
I_s	330	A	Rated current
$\omega_\mathrm{m,N}$	650	rpm	Rated mechanical speed
pp	20		Pair of poles

where λ_d and λ_q are the direct and quadrature axis flux linkages. For the calculation of dq-axis inductances defined by Eq. (4) and Eq. (5), respectively, the flux linkage variation regarding the variation of the direct and quadrature axis current excitations should be known. The current-dependent flux linkages can be determined either from the experimental test performed at locked-rotor position when the PMSM is supplied from a controller Voltage Source Inverter (VSI) or an FEA of the machine.

The PMSM under consideration is depicted in Fig. 1. The outer rotor is equipped with 40 alternately magnetized surface-mounted Neodymium-Iron-Boron (NdFeB) magnets. Besides, 36 slots shape the stator that has a two-layer distributed winding with 66 turns. The characteristic parameters of the machine are shown in Table 1.

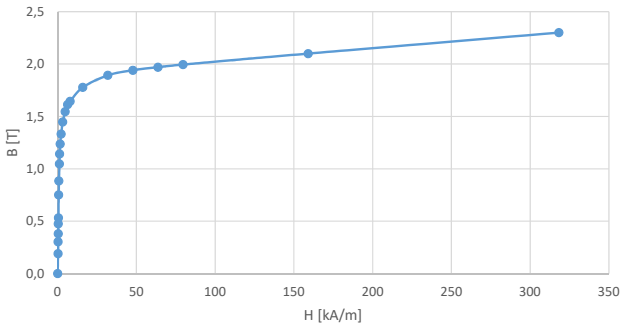

Fig. 2: Characteristic BH-curve for the electrical sheet selected for the studied machine.

The electrical sheets used for both the stator and rotor have an inherent saturation effect depicted in Fig. 2. It shows the entire characteristic BH-curve of the selected electromagnetic material. While in the range from 0 T to 1.2 T, the permeability is more or less constant, from that point on, the higher the current is, the more saturated performance is obtained.

In this paper, the determination of current-dependent flux linkage in direct and quadrature axis is obtained from a parametric setup, by using a 2D-sliced model created by Ansys-Maxwell software. The current magnitude is varied from 0 A to 330 A and the current vector angle from 0 rad to π rad. Figure 3 shows two pictures of the electric machine spinning at the rated speed where the current magnitude is zero or the maximum value at $\pi/2$ rad regarding the spatial position of the flux linkage from the magnets. While the maximum flux density achieves values between 1.6-1.8 T in the first case, when the applied current is 330 A, some parts of the machine may reach 2.1-2.3 T values. Compared with the characteristic BH-curve of the selected electrical sheet, some parts of the machine are working in the saturation area.

Authors in [4] demonstrate the correlation between the dq-axis current vector and the values of L_d and L_q, and authors in [10] present a third-order polynomial multi-variable equation system to determine

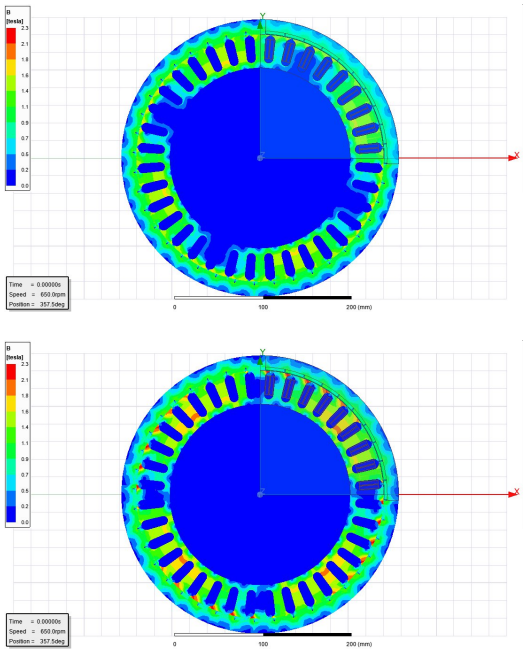

Fig. 3: Flux density distribution at rated speed at 0 A (top figure) and 330 A (bottom figure), respectively.

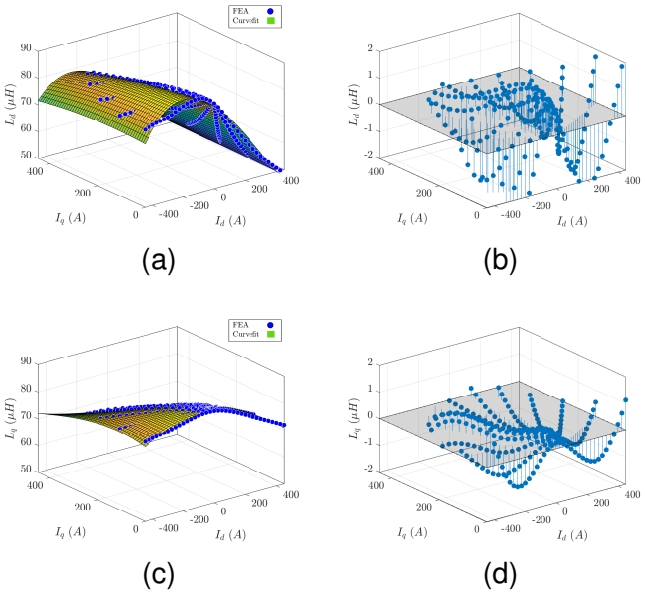

Fig. 4: Inductance fitting regarding the dq-axis currents. (a) FEA and fitted L_d. (b) Error fitting L_d. (c) FEA and fitted L_q. (d) Error fitting L_q.

this relationship as

$$[L_d, L_q] = \begin{pmatrix} 1 & I_d & I_d^2 & I_d^3 \end{pmatrix} \cdot \begin{pmatrix} a_{00} & a_{01} & a_{02} & a_{03} \\ a_{10} & a_{11} & a_{12} & a_{13} = 0 \\ a_{20} & a_{21} & a_{22} = 0 & a_{23} = 0 \\ a_{30} & a_{31} = 0 & a_{32} = 0 & a_{33} = 0 \end{pmatrix} \cdot \begin{pmatrix} 1 \\ I_q \\ I_q^2 \\ I_q^3 \end{pmatrix}, \quad (6)$$

where the $a_{x,y}$ coefficients, $\forall\,(x,y) \in [0,3]$, represent the dq-axis current order, and are calculated from the dq-axis inductances through a curve fit tool.

Figure 4 shows the inductances calculated from FEA at room temperature and the fitted ones of the 2.5 kW SPMSM studied in this paper, together with the fitting error. This figure shows that appropriate accuracy can be achieved by using Eq. (6) because this is lower than 2.5% in all current ranges.

2.2 Consideration of LBEMF and FW characteristic trajectories

The feasible trajectories are different if the sum of the back electromotive force and the winding voltage drop is lower or higher than the maximum achievable voltage from the battery power supply. Generally, for electric traction machines, the performance at the LBEMF zone is reached by following the MTPA strategy. However, in the FW zone, three regions can be differentiated depending on the torque setpoint and the mechanical speed of the machine: CT, CVL, and MTPV.

Authors in [8] have studied the characteristic curves of a PMSM in all speed ranges, but they do not consider the variation of the dq-axis inductances with the winding currents. In this paper, the optimization problem of calculating the dq-axis current references from the torque setpoint is addressed in a per-unit system to simplify the FW analysis and its implementation in a 32-bit fixed-point Digital Signal Controller (DSC).

The MTPA condition for PMSMs is defined as $\frac{\partial \tau_{\rm em}}{\partial \gamma} = 0$, which expresses the torque equation in terms of $i_{\rm s}$ and γ, where $\tau_{\rm em}$ and $i_{\rm s}$ are the electromagnetic torque and current vector modulus in the per-unit system, and γ is the current vector angle. The MTPA angle value ($\gamma_{\rm MTPA}$) is expressed as Eq. (7), where ξ is the saliency ratio calculated as $\frac{L_q}{L_d}$.

Equation (8) shows the necessary current vector modulus according to the required torque ($i_{\tau^*_{\rm em}}$), calculated from the previous value of the current vector angle and the torque reference ($\tau^*_{\rm em}$).

Finally, the MTPV trajectory is defined when the maximum torque at minimum current is achieved, considering the voltage limit. The MTPV condition for PMSMs is defined as $\frac{\partial \tau_{\rm em}}{\partial \delta} = 0$, which expresses the torque equation in terms of $v_{\rm s}$ and δ, being the voltage vector modulus and angle, respectively, in the per-unit system. Equation (9) expresses the MTPV modulus current value ($i_{\rm MTPV}$).

2.3 Consideration of inner current loop controllers

In this section, the analysis of the sensitivity of the current PI controllers is achieved based on the resistor and dq-axis inductance variation. Their stability and dynamic response are examined if the electric plant parameters are modified in terms of their nominal values. The closed-loop current transfer-function ($\mathrm{G_{CL,I}}x(\mathrm{s})$), also known as the complementary transfer-function (T(s)), can be modelled from the electric machine parameters ($R_{\rm s}$, L_x) and the parameters of the PI controllers ($K_{{\rm p},x}$, $K_{{\rm i},x}$) as

$$\mathrm{G_{CL,I}}x(\mathrm{s}) = \frac{K_{{\rm p},x}\mathrm{s} + K_{i,x}}{L_x\mathrm{s}^2 + (R_{\rm s} + K_{{\rm p},x})\,\mathrm{s} + K_{{\rm i},x}}, \quad (10)$$

where the subscript x denotes direct or quadrature axis.

Generally, the sensitivity of a closed-loop system regarding a parameter α, is defined as the ratio

$$\gamma_{\rm MTPA} = \arccos\left(\frac{-1+\sqrt{1+8i_{\rm s}^2\cdot(1-\xi(i_d,i_q))^2}}{4i_{\rm s}\cdot(1-\xi(i_d,i_q))}\right) \quad (7)$$

$$i_{\tau_{\rm em}} = \frac{-\sin(\gamma)+\sqrt{\sin(\gamma)^2+2\tau^*_{\rm em}\cdot\sin(2\gamma)\cdot(1-\xi(i_d,i_q))}}{\sin(2\gamma)\cdot(1-\xi(i_d,i_q))} \quad (8)$$

$$i_{\rm MTPV} = \frac{-(2-\xi(i_d,i_q))\cdot\cos(\gamma)-\sqrt{(2-\xi(i_d,i_q))^2\cdot\cos^2(\gamma)-4\cdot(1-\xi(i_d,i_q))\cdot(\cos^2(\gamma)\cdot(\xi(i_d,i_q)^2+1)-\xi(i_d,i_q)^2)}}{2\cdot(1-\xi(i_d,i_q))\cdot(\cos^2(\gamma)\cdot(\xi(i_d,i_q)^2+1)-\xi(i_d,i_q)^2)} \quad (9)$$

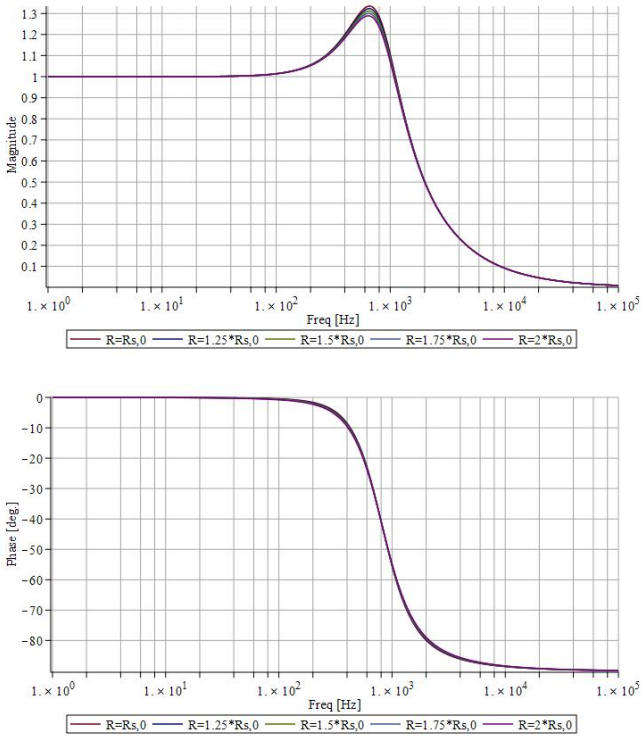

Fig. 5: Bode plot analysis of the sensitivity system varying the resistor parameter ($R_\mathrm{s} \in [R_{\mathrm{s},0}, 2R_{\mathrm{s},0}]$).

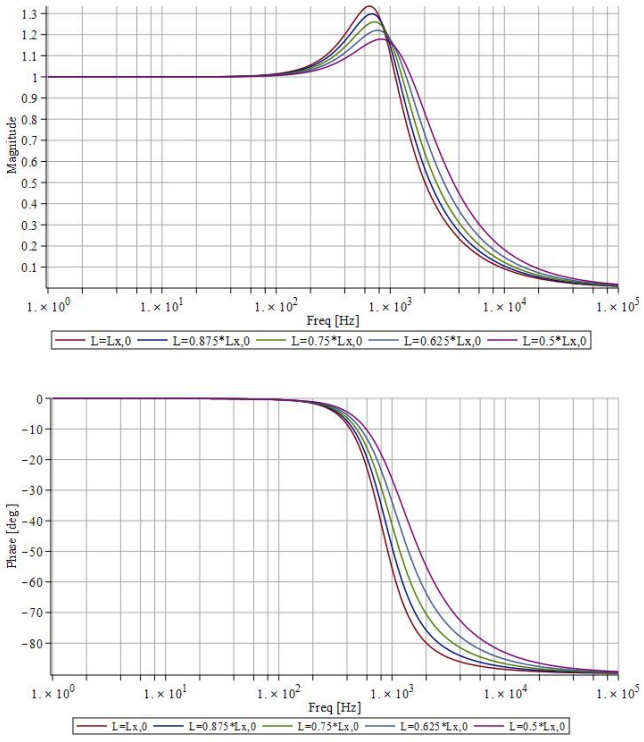

Fig. 6: Bode plot analysis of the sensitivity system varying the inductance parameter ($L_x \in [0.5 \cdot L_{x,0}, L_{x,0}]$).

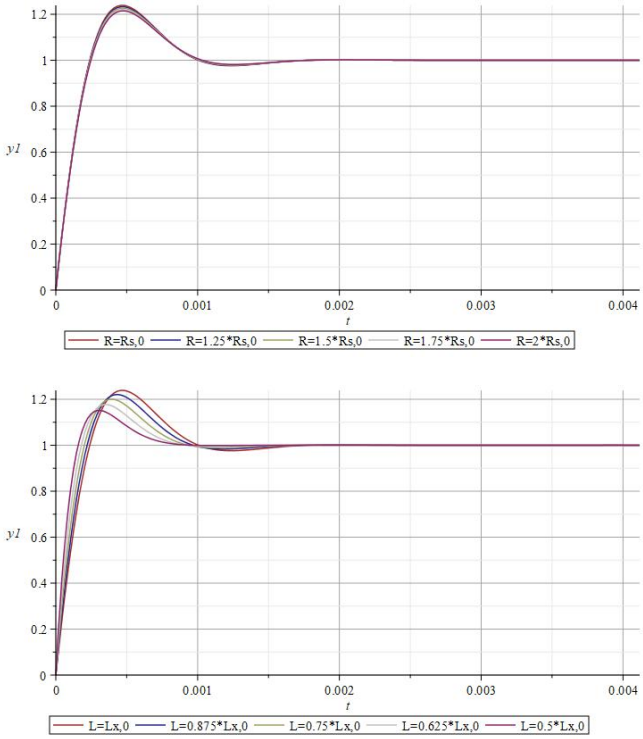

Fig. 7: Transient analysis of the sensitivity plant varying the resistor (top figure, $R_\mathrm{s} \in [R_{\mathrm{s},0}, 2R_{\mathrm{s},0}]$) and inductance (bottom figure, $L_x \in [0.5 \cdot L_{x,0}, L_{x,0}]$) parameters.

of the percentage change of the complementary transfer function to the percentage change of the parameter α evaluated at its nominal value (α_0) as

$$\mathrm{S}^{\mathrm{T}}_{\alpha}(\mathrm{s}) = \frac{\alpha}{\mathrm{T}(\mathrm{s})} \cdot \frac{\partial \mathrm{T}(\mathrm{s})}{\partial \alpha}\bigg|_{\alpha=\alpha_0} \approx \frac{\frac{\mathrm{T}(\mathrm{s})\big|_{\alpha=\alpha_{\mathrm{var}}} - \mathrm{T}(\mathrm{s})\big|_{\alpha=\alpha_0}}{\mathrm{T}(\mathrm{s})\big|_{\alpha=\alpha_0}}}{\frac{\alpha_{\mathrm{var}}-\alpha_0}{\alpha_0}}, \tag{11}$$

where the second part of the expression is the small-signal transfer-function approximation.

In case of a PMSM, the system sensitivity regarding the electrical plant parameters can be expressed from the electrical plant (evaluated in its nominal values: $R_{\mathrm{s},0}$ and $L_{\mathrm{s},0}$) and the parameters of the PI controllers as

$$\begin{aligned} \mathrm{S}^{\mathrm{T}}_{R_\mathrm{s}}(\mathrm{s}) &\approx \frac{R_\mathrm{s}}{\mathrm{T}(\mathrm{s})} \cdot \frac{\Delta \mathrm{T}(\mathrm{s})}{\Delta R_\mathrm{s}}\bigg|_{\substack{R_\mathrm{s}=R_{\mathrm{s},0} \\ L_x=L_{x,0}}} \\ &= \frac{-R_{\mathrm{s},0} \cdot \mathrm{s}}{L_{x,0} \cdot \mathrm{s}^2 + (R_{\mathrm{s},0} + K_{\mathrm{p},x}) \cdot \mathrm{s} + K_{\mathrm{i},x}} \end{aligned} \tag{12}$$

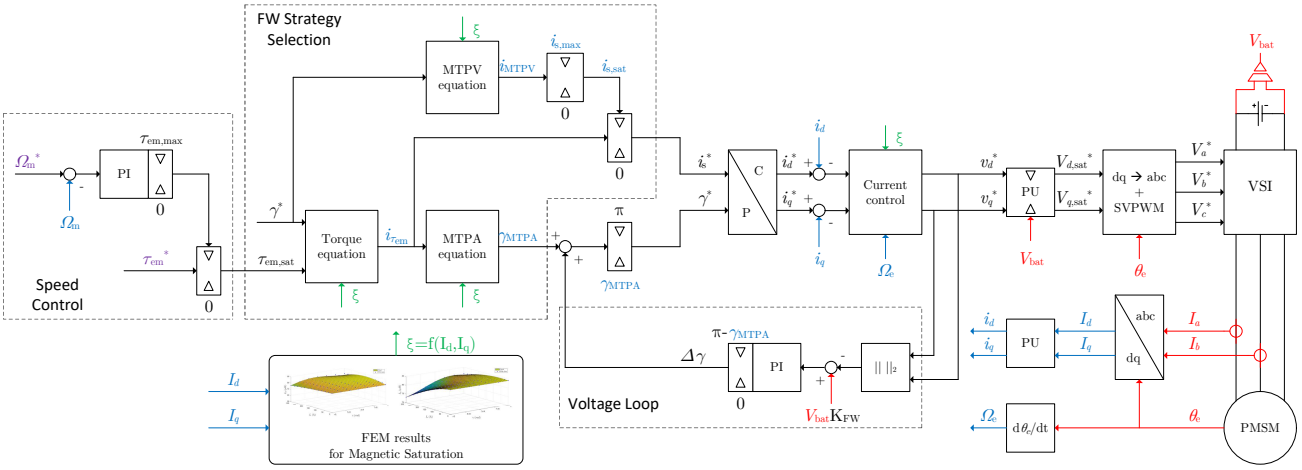

Fig. 8: Control algorithm model. The magnetic saturation, represented in green, affects both the LBEMF and FW trajectories and cross-terms of the current PI controllers. The reference, feedback and intermediate values are depicted in purple, red, and blue, respectively.

$$\mathrm{S}^{\mathrm{T}}_{L_x}(\mathrm{s}) \approx \frac{L_x}{\mathrm{T}(\mathrm{s})} \cdot \frac{\Delta \mathrm{T}(\mathrm{s})}{\Delta L_x}\bigg|_{\substack{R_\mathrm{s}=R_{\mathrm{s},0} \\ L_x=L_{x,0}}} = \frac{-L_{x,0} \cdot \mathrm{s}^2}{L_{x,0} \cdot \mathrm{s}^2 + (R_{\mathrm{s},0} + K_{\mathrm{p},x}) \cdot \mathrm{s} + K_{\mathrm{i},x}} \tag{13}$$

Due to thermal considerations, the resistance of the stator winding is higher than its nominal value. Due to the saturation effect, the stator winding's inductances are considered lower than their current values equal to zero. The Bode analysis of the complementary sensitivity transfer-function regarding the variation of the resistor and inductance values considered in Table 1 is shown in Fig. 5 and Fig. 6, respectively. The phase margin varies very little in both cases. Furthermore, transient response in front of a unitary step is analysed in Fig. 7. In these figures, it can be demonstrated that the control algorithm is stable whenever the variation of the winding resistance or inductances occurs, and the system dynamic is not greatly affected.

3 Simulation Results

The proposed control algorithm, which is shown in Fig. 8, is validated by means of a MATLAB/Simulink model. It considers the saturation effects in all torque-speed regions, by affecting both the trajectories at the LBEMF and FW zones. Ω^*_m and Ω_m are the reference and current mechanical speed, respectively, and Ω_e is the current electrical speed in the per-unit system. The output of the speed controller limits the maximum reference setpoint ($\tau_{\mathrm{em,max}}$). MTPA, electromagnetic torque, and MTPV equations refer to Eq. (7)-Eq. (9), respectively. The output voltage modulus is controlled so as to transition between the LBEMF and FW zones by changing the current vector angle ($\Delta\gamma$). The maximum output voltage value is limited to a constant parameter (K_FW) and the current battery voltage (V_bat).

An optimised calculation of the working-point trajectory is done in the per-unit system to simplify its implementation in a real 32-bit fixed-point DSC. For this purpose, the field-oriented control is addressed by i_{dq}, v_{dq}, i^*_{dq}, and v^*_{dq}, which are the current and voltage real and reference values in the per-unit system.

Figure 9 depicts the comparison of the MTPA (green), CT (magenta), and MTPV (yellow) trajectories by taking into account the constant dq-axis inductances at zero current (solid lines) and the variable values with the dq-axis currents (dashed lines). The current circle limit is shown in red. Due to the saliency ratio variation below 1, the hyperbolas of MTPA and MTPV change their direction.

Figure 10 shows the increase of the applied torque to the machine when the saturation effects are considered, by taking as a base value the torque gotten with constant dq-axis inductances. This comparison is made when the electric machine is working in the MTPA region. At 330 Nm, a torque increase of 1%

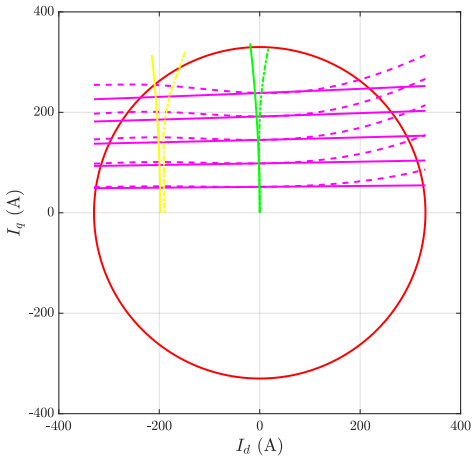

Fig. 9: MTPA (green), CT (magenta), and MTPV (yellow) trajectories not considering the cross-saturation effects (solid line) and considering them (dashed line).

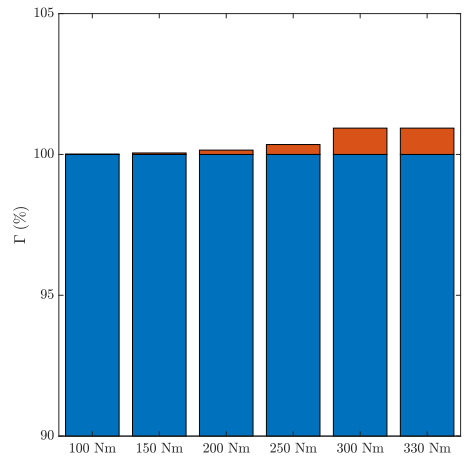

Fig. 10: Attainable torques without and with the cross-saturation effects at the MTPA region, from 100 Nm up to 330 Nm, are depicted in blue and orange, respectively.

is achieved when considering the cross-saturation effects.

Figure 11 depicts the transient working-point of the proposed control algorithm when a reference torque of 300 Nm with a limited speed of 700 rpm is applied. The current and voltage limits at the maximum speed are represented in red and blue, respectively. MTPA and MTPV curves are illustrated in green and yellow, respectively. Torque reference curve is depicted in magenta. Solid cyan represents the working-point going from the LBEMF zone, working in the MTPA zone, up to the FW zone, working in the CT, CVL, MTPV regions, and constant speed. In comparison, the black line represents the working-point when the saturation effects are not considered in the control algorithm. In conclusion, the best efficiency is accomplished as long as the cross-magnetization effects are considered.

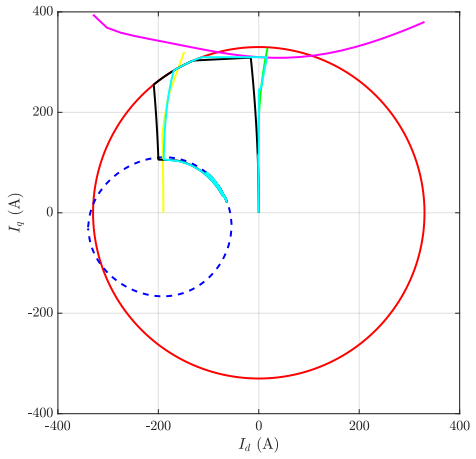

Fig. 11: Transient working point applying a torque set-point of 300 Nm and limiting the maximum speed to 700 rpm.

4 Conclusion

This paper proposes an advanced FW control algorithm based on a VCC strategy that considers the saturation effects on the electromagnetic sheets to calculate the optimised working-point and analyses the dynamic of the PI current controllers. The sensitivity analysis which was done taking into consideration a variation of the electric machine resistor or inductances has not proven any significance in the dynamic response of the inner control loops.

Nevertheless, the simulation results prove the effectiveness of considering the saturation effects in calculating the dq-axis current from the torque or speed reference. In case of the 2.5 kW SPMSM analysed, located in a direct drive e-motorbike, whose saliency ratio is barely less than 0.96 at the maximum current, the torque increase is up to 1%.

Acknowledgements

This project has received funding from the European Union's Horizon 2020 research and innovation program under grant agreement No 814958.

References

[1] B. Bilgin, P. Magne, P. Malysz, Y. Yang, V. Pantelic, *et al.*, "Making the Case for Electrified Transportation," *IEEE Transactions on Transportation Electrification*, vol. 1, no. 1, pp. 4–17, 2015. DOI: 10.1109/TTE.2015.2437338.

[2] L. Sepulchre, M. Fadel, M. Pietrzak-David, and G. Porte, "Flux-weakening strategy for high speed PMSM for vehicle application," in *2016 International Conference on Electrical Systems for Aircraft, Railway, Ship Propulsion and Road Vehicles and International Transportation Electrification Conference, ESARS-ITEC 2016*, 2016, pp. 1–7. DOI: 10.1109/ESARS-ITEC.2016.7841413.

[3] S. M. S. I. Shakib, S. Member, D. Xiao, R. Dutta, K. S. Alam, *et al.*, "An Analytical Approach to Direct Torque and Flux Control of Interior Permanent Magnet Synchronous Machine for Deep Field Weakening Without Using Pre-calculated Lookup Tables," in *10th International Conference on Power Electronics - ECCE Asia*, IEEE, 2019, pp. 1–6.

[4] S. Wang, J. Kang, M. Degano, A. Galassini, and C. Gerada, "An Accurate Wide-Speed Range Control Method of IPMSM Considering Resistive Voltage Drop and Magnetic Saturation," *IEEE Transactions on Industrial Electronics*, vol. 67, no. 4, pp. 2630–2641, 2020. DOI: 10.1109/tie.2019.2912766.

[5] L. Huang, C. Zhao, and P. Huang, "An approach to improve the torque performance of IPMSM by considering cross saturation applied for hybrid electric vehicle," in *2010 International Conference on Electrical Machines and Systems, ICEMS2010*, IEEE, 2010, pp. 1378–1381.

[6] L. Sepulchre, M. Fadel, and M. Pietrzak-David, "MTPV for continuous flux-weakening strategy control law for IPMSM," in *SPEEDAM 2018 - Proceedings: International Symposium on Power Electronics, Electrical Drives, Automation and Motion*, IEEE, 2018, pp. 1221–1226. DOI: 10.1109/SPEEDAM.2018.8445329.

[7] J. Ottosson and M. Alaküla, "A compact field weakening controller implementation," *International Symposium on Power Electronics, Electrical Drives, Automation and Motion, 2006. SPEEDAM 2006*, vol. 2006, no. 1, pp. 696–700, 2006. DOI: 10.1109/SPEEDAM.2006.1649859.

[8] C. Miguel-espinar, D. Heredero-peris, G. Gross, M. Llonch-masachs, D. Montesinos-miracle, and F. Member, "Maximum Torque per Voltage Flux-Weakening strategy with speed limiter for PMSM drives," *IEEE Transactions on Industrial Electronics*, vol. 0046, pp. 1–11, 2020. DOI: 10.1109/TIE.2020.3020029.

[9] R. Krishnan, *Permanent Magnet Synchronous and Brushless DC Motor Drives*, Taylor and Francis Group, Ed. Virgina, USA: CRC Press, 2010, pp. 303–327.

[10] R. Ni, D. Xu, G. Wang, L. Ding, G. Zhang, and L. Qu, "Maximum Efficiency per Ampere Control of Permanent-Magnet Synchronous Machines," *IEEE Transactions on Industrial Electronics*, vol. 62, no. 4, pp. 2135–2143, 2015. DOI: 10.1109/TIE.2014.2354238.